Mesospheric CO_2 ice clouds on Mars observed by Planetary Fourier Spectrometer onboard Mars Express

S. Aoki[a,b,c,d,*], Y. Sato[c], M. Giuranna[d], P. Wolkenberg[d,e], T. M. Sato[f], H. Nakagawa[c], and Y. Kasaba[c]

[a] Belgian Institute for Space Aeronomy (IASB-BIRA), Ringlaan-3-Avenue Circulaire, Uccle 1180, Brussels, Belgium.

[b] Fonds National de la Recherche Scientifique (FNRS), 5 rue d'Egmont, B-1000 Brussels, Belgium

[c] Department of Geophysics, Graduate school of Science, Tohoku University, Aramaki Aza Aoba

[d] Istituto di Astrofisica e Planetologia Spaziali (IAPS), Istituto Nazionale di Astrofisica (INAF), Via del Fosso del Cavaliere 100, 00133 Rome, Italy.

6-3, Aoba, Sendai, Miyagi 980-8578, Japan.

[e] Centrum Badań Kosmicznych Polskiej Akademii Nauk (CBK-PAN), ul. Bartycka 18A, 00-716 Warszawa, Poland

[f] Institute of Space and Astronautical Science (ISAS), Japan Aerospace Exploration Agency (JAXA), 3-1-1, Yoshinodai, Chuo-ku, Sagamihara, Kanagawa 252-5210, Japan.

Mars; Mars, atmosphere; Mars, climate; Infrared observations; Spectroscopy

Corresponding author:

Shohei Aoki

Belgian institute for Space Aeronomy (IASB-BIRA), Ringlaan-3-Avenue Circulaire, Uccle 1180, Brussels, Belgium.

E-mail: shohei.aoki@aeronomie.be

Abstract

We have investigated mesospheric CO_2 ice clouds on Mars through analysis of near-infrared spectra acquired by Planetary Fourier Spectrometer (PFS) onboard the Mars Express (MEx) from MY 27 to MY 32. With the highest spectral resolution achieved thus far in the relevant spectral range among remote-sensing experiments orbiting Mars, PFS enables precise identification of the scattering peak of CO_2 ice at the bottom of the 4.3 μm CO_2 band. A total of 111 occurrences of CO_2 ice cloud features have been detected over the period investigated. Data from the OMEGA imaging spectrometer onboard MEx confirm all of PFS detections from times when OMEGA operated simultaneously with PFS. The spatial and seasonal distributions of the CO_2 ice clouds detected by PFS are consistent with previous observations by other instruments. We find CO_2 ice clouds between *Ls* = 0° and 140° in distinct longitudinal corridors around the equatorial region (± 20°N). Moreover, CO_2 ice clouds were preferentially detected at the observational LT range between 15–16 h in MY 29. However, observational biases prevent from distinguishing local time dependency from inter-annual variation. PFS also enables us to investigate the shape of mesospheric CO_2 ice cloud spectral features in detail. In all cases, peaks were found between 4.240 and 4.265 μm. Relatively small secondary peaks were occasionally observed around 4.28 μm (8 occurrences). These spectral features cannot be reproduced using our radiative transfer model, which may be because the available CO_2 ice refractive indices are inappropriate for the mesospheric temperatures of Mars, or because of the assumption in our model that the CO_2 ice crystals are spherical and composed by pure CO_2 ice.

1. Introduction

One of the peculiar phenomena of the Martian climate is the existence of carbon dioxide (CO_2) ice clouds. These clouds are formed by condensation of the major constituent of the Martian atmosphere, CO_2. Recent observations have revealed the presence of the CO_2 ice clouds at remarkably high altitudes (above 40 km; mesosphere). The existence of mesospheric CO_2 ice clouds on Mars was first suggested by the infrared spectra recorded by Mariner 6 and 7 (Herr and Pimentel, 1970) although the low altitude of the detection (25 km) argues in favor of CO_2 fluorescence (e.g Lellouch et al., 2000). Clancy and Sandor et al. (1998) discussed the mesospheric CO_2 ice clouds formation based on vertical temperature profiles measured by Pathfinder during its descent (Schofield et al., 1997) and those by the James Clerk Maxwell Telescope. Subsequently, Montmessin et al. (2006) detected several mesospheric detached layers at an altitude of around 100 km at [32°S, −178°E, Ls = 134°], [36°S, 134°E, Ls = 135°], [15°S, 15°E, Ls = 137°], and [15°S, −83°E, Ls = 137°] from the nighttime measurements by SPectroscopy for the Investigation of the Characteristics of the Atmosphere of Mars (SPICAM) ultraviolet (UV) channel onboard Mars Express (MEx). These detached layers were attributed to the presence of CO_2 ice crystals because of the simultaneous detection of a supersaturated cold pocket just above the aerosol layer.

A global view of these mesospheric CO_2 ice clouds has been provided by Observatoire pour la Minéralogie l'Eau les Glaces et l'Activité (OMEGA) onboard MEx and the Compact Reconnaissance Imaging Spectrometer for Mars (CRISM) onboard Mars Reconnaissance Orbiter (MRO) daytime observations (Montmessin et al., 2007; Määttänen et al., 2010; Vincendon et al., 2011). From the OMEGA data, mesospheric CO_2 ice clouds were identified through a more straightforward approach. A distinct peak was detected at the bottom of the 4.3-μm CO_2 gas band, caused by scattering of CO_2 ice cloud crystals in the mesosphere (Montmessin et al., 2007). The fundamental ν_3 band of CO_2 ice is possibly the strongest known infrared band for a molecule (Warren, 1986), and the combination of the dramatic increase of the imaginary part of the CO_2 ice index and large fluctuation of the real part produces a sharp peak around 4.26 μm. From the OMEGA data analysis, a total of 60 occurrences were identified during the period from MY 27 to 29 (Määttänen et al., 2010) and 13 occurrences in MY 30 (Vincendon et al., 2011). Additionally, CRISM daytime measurements detected the mesospheric CO_2 ice clouds via indirect spectral identification. Although CRISM is a similar instrument to OMEGA, it does not observe the distinctive scattering peak at the bottom of the 4.3 μm CO_2 band because of its limited spectral range (0.362–3.92 μm). Instead, cloud features were identified from the CRISM RGB composite images (based on wavelengths of 0.592, 0.533, and 0.492 μm), and CO_2 ice clouds were distinguished from H_2O ice based on the CRISM IR spectra. From the CRISM observations during the period from MY 29 to MY 30, 54 occurrences in total were found (Vincendon et al., 2011). These detections by OMEGA and CRISM are mainly within a distinct longitudinal corridor (−120°E to +30°E) around the equatorial region (20°S to 20°N) during the aphelion season (Ls = 330–150°), with the exception of two detections by OMEGA at mid-latitudes at [49.1°S, −138.3°E, Ls = 54.2°] and [46.6°N, −74.7°E, Ls = 246.3°], one detection by CRISM around 155°E, and one by OMEGA around 120°E.

The formation mechanism of the mesospheric CO_2 ice clouds has been discussed based on the observed spatial and seasonal distributions. Clancy and Sandor (1998) first suggested a scenario whereby the clouds form in supersaturated pockets of air created by the interference of thermal tides and gravity waves. This scenario has been demonstrated by theoretical studies. González-Galindo et al. (2011) showed using a Mars Global Circulation Model that the observed mesospheric CO_2 ice clouds can be found in places where temperature minima are reached in the atmosphere due to the propagation of thermal tides. This study showed that observations were significantly correlated with the seasonal and spatial distributions of these minima caused by the propagation of the large-scale waves, even though the temperature remained just above the condensation threshold. Subsequently, Spiga et al. (2012) showed using a mesoscale model that the locations where clouds are observed are places where gravity waves are not filtered by Martian atmospheric dynamics and can propagate upward into the mesosphere. This study supported the inference that smaller-scale waves allow the creation of supersaturated pockets in the temperature minima created by the thermal tides. Finally, Listowski et al. (2014) demonstrated that temperature profiles that combine the effects of thermal tides and gravity waves in a one-dimensional microphysical bin model enable simulation of mesospheric CO_2 ice clouds that are consistent with observations.

The crystal size of the mesospheric CO_2 ice clouds was constrained by the spectroscopic observations. SPICAM-UV nighttime observations suggested that the effective radii of the CO_2 cloud crystals detected around 100 km are between 0.08 and 0.13 μm (Montmessin et al., 2006). In contrast, larger crystal sizes were estimated from the daytime observations at lower altitudes (~60-80 km) by OMEGA and CRISM. The OMEGA analysis showed that crystal radii are within 1–3 μm, and that their optical depths are between 0.01 and 0.6 at λ = 1 μm (Määttänen et al., 2010); the CRISM analysis showed that crystal radii are within 0.5–2 μm and, that their optical depths are lower than 0.3 at λ = 0.5 μm (Vincendon et al., 2011). These estimates were calculated by comparing the measurements and simulations based on the Mie theory (with spherical particle shape assumed). Note that in the OMEGA data analysis, the peak at 4.3 μm was not used directly; the crystal size was derived from ratios between the radiances inside and outside shadows. While understanding of the exact composition of the cloud crystals (pure CO_2 ice or not) and their shapes in the clouds are still poor because there are not direct observations.

In this study, we have investigated these mesospheric CO_2 clouds using the nadir near-infrared spectra of the Planetary Fourier Spectrometer (PFS) onboard MEx. To date, PFS has the highest spectral resolution in the 4.3 μm CO_2 band. Using this unique dataset, a detailed study has been conducted on the spectral position, shape, and intensity of the CO_2 ice cloud scattering peak around 4.3 μm. The high-spectral-resolution observations of PFS provide not only a new dataset to compare with previous observations but also new insights into the optical properties of the mesospheric CO_2 ice clouds (such as crystal size, composition, and shape). The details of the PFS data analysis are described in Section 2. The observational results are presented in Section 3. A comparison between the spectra measured by PFS and synthetic spectra from a radiative transfer model is provided in Section 4, and the results are discussed in Section 5. Finally, concluding remarks are provided in Section 6.

2. PFS Data Analysis

2.1. Planetary Fourier Spectrometer (PFS)

PFS is a Fourier transform spectrometer onboard the MEx orbiter optimized for atmospheric studies (Formisano et al., 2005). It has two spectral channels: the Short Wavelength Channel (SWC, 2000–8600 cm^{-1}) and the Long Wavelength Channel (LWC, 250–1700 cm^{-1}). The fields of view are 1.6° for the SWC and 2.8° for the LWC. Both channels have a spectral sampling step of 1.0 cm^{-1} and a spectral resolution of 1.3 cm^{-1}. The spectral and radiometric calibration procedure for both channels has been discussed in detail by Giuranna et al. (2005a, b). An advantage of PFS is its wide spectral coverage coupled with its relatively high spectral resolution. In about six

Martian years, PFS has collected more than 2,500,000 spectra for each channel. With full spatial coverage every year, PFS has been sounding the Martian atmosphere at different local times and seasons, which enables investigation of the diurnal, seasonal, and inter-annual variability of several atmospheric constituents and optical parameters of aerosols.

2.2. Searching for mesospheric CO_2 ice cloud features with PFS

In this study, we have analyzed PFS spectra collected over a period of about six Martian years, from July 2004 to March 2015 (MEx Orbit #634–14454), which corresponds to the beginning of MY 27 and the end of MY 32, respectively. To detect mesospheric CO_2 ice clouds, the scattering peak of CO_2 ice at the bottom of the 4.3 μm CO_2 band in the SWC spectra was searched. Because the lines of this strong CO_2 band are saturated, no solar reflection signal is expected between 4.2 and 4.5 μm, except in the following three cases (Montmessin et al., 2007): (1) solar reflection from high topographic regions (i.e., partial desaturation of the CO_2 band), (2) non-local thermodynamic equilibrium (non-LTE) emission of CO_2 and CO, and (3) solar reflection by high-altitude aerosols, such as mesospheric CO_2 ice clouds. In the first case, an emission-like feature gradually appears around 4.38 μm with increasing surface altitude because of the weaker amplitudes of the CO_2 absorption lines at that wavelength (Rothman et al., 2013). The second case typically occurs in PFS limb observations, when non-LTE spectral features appear within a wide spectral range between 4.15 and 4.5 μm (Formisano et al., 2006). As we are only interested in the mesospheric CO_2 ice clouds, we carefully selected nadir-only observations with emission angles lower than 30° and relative to surface altitudes lower than 8 km. These criteria exclude limb observations and guarantee saturation of the 4.3-μm band.

We built an algorithm to detect mesospheric CO_2 ice clouds from the PFS spectra. In this algorithm, two parameters (d_1 and d_2) were introduced:

$$d_1 = \max\left\{I_{PFS}(\lambda) - I_0(\lambda)\right\}_{\lambda=4.22-4.35\mu m},$$

$$d_2 = \frac{1}{d}\sum_{\lambda=4.22\mu m}^{4.35\mu m}\left(\frac{I_{PFS}(\lambda) - F(\lambda)}{\sigma(\lambda)}\right)^2,$$

where I_{PFS} is the PFS radiance smoothed with five spectral points (to improve the signal to noise ratio); I_0 is the background radiance between 4.22 and 4.35 μm, which was estimated by linear regression from the two spectral ranges at 4.20–4.22 and 4.35–4.37 μm; F is the best-fit quadratic function with the smoothed PFS radiance for wavelengths within the range of 4.22–4.35 μm; d is the degree of freedom in the fitting (i.e., the number of spectral points N in the wavelength range 4.22–4.35 μm minus 2); and σ is the noise equivalent radiance (NER) of PFS. The first parameter, d_1, is the maximum radiance at wavelengths between 4.22 and 4.35 μm, which is used to identify the scattering peak of CO_2 ice at the bottom of the 4.3 μm CO_2 band. To derive this parameter, the deviation of the smoothed PFS spectra (I_{PFS}) from the background radiance (I_0) is calculated for the spectral range 4.22–4.35 μm. The second parameter, d_2, is a reduced chi-square value of the quadratic polynomial fit to I_{PFS} at wavelengths between 4.22 and 4.35 μm, which is used to distinguish the data with spectral features of CO_2 ice clouds from those with relatively large noise. To derive this parameter, a quadratic function was applied to the smoothed PFS spectra (I_{PFS}) for wavelengths between 4.22 and 4.35 μm. Spectra were selected as possible candidates for showing CO_2 ice cloud features if their d_1 value was three time larger than their NER value (~0.013 erg/sr/cm^2/cm^{-1}) and if their d_2 value was larger than 1.2. Then, possible candidates for CO_2 cloud features were screened visually to check if they are associated with high topography or instrumental problems. This algorithm and the threshold values for d_1 and d_2 were obtained from experimental tests using spectra from orbit #5267. During that orbit, both PFS and OMEGA operated simultaneously (both onboard MEx), and OMEGA detected extensive mesospheric CO_2 ice clouds (Määttänen et al., 2010).

Figure 1a shows a typical dayside spectrum of PFS in the spectral range between 4.0 and 4.5 μm, which has no CO_2 ice cloud features ($d_1 < 0.039$, $d_2 < 1.2$). About 96.93% of the PFS spectra in the selected dataset do not have any particular features at the bottom of the 4.3 μm CO_2 band (i.e., $d_1 < 0.039$, $d_2 < 1.2$), such as the spectrum shown in **Fig. 1a**. In contrast, the two spectra shown in **Figs. 1b** and **1c** indicate CO_2 ice cloud features, which are identified by the algorithm (i.e., $d_1 > 0.039$, $d_2 > 1.2$). In total, 111 occurrences of such mesospheric CO_2 ice cloud features were identified, which constitutes about 0.01% of the spectra in the selected dataset. Note that one of the two examples has a secondary peak around 4.28 μm (**Fig. 1c**), although these two spectra were obtained at almost the same region and time. This secondary peak has not previously been reported because the spectral resolution of OMEGA cannot resolve this feature. The small secondary peak was observed in about eight occurrences in total. The rest of the PFS spectra (i.e., 3.06% of the spectra in the selected dataset) have high maximum radiance ($d_1 > 0.039$) but low chi-square values ($d_2 < 1.2$) because of relatively large noise. **Fig. 1d** shows an example of these cases. As shown in this figure, the relatively large noise provides a large d_1 value, although a distinct scattering peak is not visible. To exclude such cases, the second parameter, d_2, is introduced in the algorithm.

Table 1 provides a list of the mesospheric CO_2 ice clouds detected from the selected PFS data using the algorithm. We compared these detections with those reported by OMEGA measurements during MY 27–30 for validation (Tables 3 and 4 in Määttänen et al., 2010; Table 3 in Vincendon et al., 2011). During a period of simultaneous operation between OMEGA and PFS in MY 27-30, 100% of the PFS detections were also confirmed by the OMEGA data (51 cases), which demonstrates that this algorithm is robust enough to detect these cloud features. However, the algorithm is not optimized for weak signals, such as optically thin clouds or small clouds (relative to the PFS-FOV). **Fig. 1e** shows one of the spectra without CO_2 ice cloud features classified by the algorithm (d_1 < 0.039, d_2 < 1.2) but with possible CO_2 ice cloud features around 4.25 μm. Although developing a robust algorithm to detect such weak signal is not a trivial task, such occurrences can be detected by eye. After visual inspection of the entire PFS dataset, we identified an additional 175 occurrences of CO_2 ice clouds, as described and listed in the **Appendix A**.

3. Spatial, seasonal, and local time distributions

Figure 2 shows the spatial and seasonal distributions of the mesospheric CO_2 ice clouds detected in PFS spectra with the algorithm described in Section 2. CO_2 ice clouds were detected within a longitudinal range of −100.6°E to +23.2°E (109 cases) and around +161°E (two cases) over equatorial latitudes from 15.6°S to 21.5°N, and in the seasonal range between *Ls* = 8.9° and 134.6°. Most of these clouds occurred between *Ls* = 10° and 30° (87 cases). The locations and season in which mesospheric CO_2 ice clouds were detected are consistent with previous spectroscopic observations by OMEGA and CRISM (Montmessin et al., 2007; Määttänen et al., 2010; Vincendon et al., 2011). In particular, the distributions shown by the PFS data are similar to those observed by CRISM (Vincendon et al., 2011). No CO_2 ice clouds were detected from the PFS data at mid-latitudes, where both SPICAM and OMEGA have detected such clouds. SPICAM observed two occurrences of such mid-latitudes clouds around [32°S, −178°E] (LT = 1:00) and [36°S, +134°E] (LT = 24:00) at *Ls* = 134–135° (Montmessin et al., 2006). It is reasonable to infer that PFS could not detect such clouds because these were detected by SPICAM in nighttime, whereas PFS measurements are performed in daytime. Moreover, the effective crystal radii of the CO_2 ice clouds detected by SPICAM were estimated to be between 0.08 and 0.13 μm (Montmessin et al., 2006), and our radiative transfer calculations suggest that no scattering peak forms at the bottom of the 4.3-μm band with such small crystals (see Section 4 and **Fig. 5**). In contrast, OMEGA identified two mid-latitude clouds based on the scattering peak of CO_2 ice at 4.3 μm from daytime observations around [46.6°N, −74.7°E] at *Ls* = 246.4° (LT = 14.1) and [49.1°S, −138.3°E] at *Ls* = 54.2° (LT = 7.9) (Määttänen et al., 2010). Unfortunately, PFS did not conduct simultaneous observations with OMEGA for these detected mid-latitudes clouds. As shown in **Fig. 6** of Määttänen et al. (2010), the horizontal scale of the mid-latitude clouds is about 35 km. In principle, such clouds can be detected even with the relatively large FOV of PFS (about 7 km at the pericenter). Note that even by eye, mid-latitudes CO_2 clouds could not be found in the PFS dataset (see **Appendix A**). The PFS and OMEGA results suggest that the presence of CO_2 clouds at mid-latitudes is an unusual event.

As shown in **Fig. 3a**, PFS measurements have different local times (LT) for each MY because of the non-Sun-synchronous orbit of MEx. **Fig. 3b** shows the number of the mesospheric CO_2 ice cloud detections of PFS with the corresponding observational LT and MY. We detected mesospheric CO_2 ice clouds at local times between 8.3 and 17.9 h, except during 10–11 h, with a maximum at 15–16 h. The low radiance before 8 h and after 18 h did not allow detection of the clouds. The previous OMEGA study detected clouds between 7.9 and 17.3 h except during 12–13 h (Määttänen et al., 2010). To investigate the LT dependence of mesospheric CO_2 ice clouds, the detection probability for a given LT, which is equal to the number of mesospheric CO_2 ice cloud detections at that LT divided by the total number of measurements at that LT, was calculated at 1-h intervals for local times between 8 and 18 h. The PFS observations within the latitudinal range of

20°S to 20°N, the longitudinal range of −110°E to +30°E, and the solar longitudinal range of 10° to 30° were used for this calculation to reduce the effects of spatial and seasonal dependence of the observational local time. **Fig. 3c** shows the resulting detection probability of mesospheric CO_2 ice clouds. As shown in this figure, we have found that mesospheric CO_2 ice clouds are preferentially detected in spectra taken in the late afternoon (15–16 h), which were all measured in MY 29. Määttänen et al. (2010) also reported that numerous clouds were detected around 15–16 h in the OMEGA data collected in MY 29. In the PFS dataset, the CO_2 clouds are most frequently observed around 15-16 LT and/or in MY29 for the 20°S-20°N band, and for the Ls=10-30°, however this conclusion cannot be generalized because of the significant inter-annual variations in observational coverage because of the non-Sun-synchronous orbit of MEx.

Gonzalez-Galindo et al. (2011) showed that the minima of temperature due to the thermal tides in their GCM occur at local times/altitudes where mesospheric clouds were observed. Thus, the local time formation for the cloud seems to be determined by the local time of the temperature minima of the thermal tides (as for the spatial distribution of the clouds). However, no detailed cloud simulation work investigated the full diurnal cycle of mesospheric CO_2 cloud formation.

During the northern fall season of MY 28, global dust storm occurred on Mars (Smith, 2009; Wolkenberg et al., 2017). Listowski et al. (2014) discussed possible contribution from a dust storm to the formation of the mesospheric CO_2 ice clouds. They calculated the sedimentation rates and the resulting dust size vertical distribution for the full dust size distribution with a radius grid ranging from 1 nm to 100 micrometers. The calculated dust number densities are small that their effect on the formation of observable clouds is negligible or cannot dominate during the full MY29 cloud season (Listowski et al., 2014). It does not support that the increase of CO_2 clouds detections in MY 29 is due to the global dust storm occurred in MY 28.

We can partially constrain the altitude of the detected CO_2 ice clouds based on temperature profiles retrieved from PFS thermal-infrared data which allow retrievals of the atmospheric temperatures from 0 to 50 km from the 15-μm CO_2 band (e.g., Grassi et al., 2005a). The uncertainty of the retrieved vertical temperature profile is less than 2 K at 5–20 km and increases to 7 K at 50 km, and nadir view of the 15-μm CO_2 band is not sensitive temperature above 50 km (Grassi et al., 2005b). Comparison between the measured temperature profiles and CO_2 condensation temperatures reveals that temperatures below the altitude of 50 km do not fall below the condensation temperature, which confirms that the detected CO_2 ice clouds occur above 50 km.

4. Comparison with synthetic spectra from a radiative transfer model

We have performed radiative transfer calculations to reproduce the spectral shapes of the mesospheric CO_2 ice clouds measured by PFS. We used a fast and accurate radiative transfer model that includes multiple scattering effects (Ignatiev et al., 2005). CO_2 ice clouds and CO_2 gas are taken into account in the calculations, and the model atmosphere is divided into 100 layers with uniform thicknesses of 1 km. The single scattering parameters (i.e., extinction coefficient, single-scattering albedo, and scattering phase function) of the CO_2 ice clouds were calculated with the Mie theory based on the assumption of a spherical particle shape (Wiscombe, 1980). The Mie theory calculation requires refractive indices as an input parameter. To date, two measurements of the refractive indices of CO_2 ice have been made under temperatures relatively close to those of the Martian mesosphere; one of these was the measurement of Warren (1986) taken at 65–80 K (hereafter "Warren RI"), and the other was that of Wood and Roux (1982) taken at 80 K (hereafter "Wood RI"). **Fig. 4** compares these refractive indices in the spectral range between 4.20 and 4.42 μm. Both of these indices were tested for this study. For the size distribution of CO_2 ice crystals, a lognormal distribution was adopted. The absorption coefficients of CO_2 gas were calculated based on the line-by-line method with a spectral sampling of 0.0003 cm^{-1} using the HITRAN 2012 database (Rothman et al., 2013). For the line shape function of the gas, a Voigt function was adopted (Kuntz, 1997; Ruyten, 2004). We used the solar spectrum obtained by Fiorenza and Formisano (2005). Surface albedo was assumed to be independent of wavelength and set to 0.15. Although surface albedo is variable with area, it does not impact the spectral shape at the bottom of the 4.3 μm CO_2 band because the reflection of solar radiance from the surface is completely absorbed by CO_2 gas in the cases selected for this study.

We assumed that the spectral feature of the mesospheric CO_2 ice clouds at the bottom of the 4.3-μm CO_2 band could be reproduced through variation of the following three parameters: optical depth τ of CO_2 clouds (reference wavelength: 1 μm), effective radius r_{eff}, and effective variance v_{eff}. The synthetic spectra were computed for combinations of the following parameters: τ = [0.01, 0.1, 0.3, 0.6, 0.9, 1.2]; r_{eff} = [0.1, 0.5, 1.0, 3.0 μm]; v_{eff} = [0.1, 0.5, 1.0]. Based on the previous observations, we have considered three scenarios with clouds distributed uniformly within three ranges of altitudes (Scholten et al., 2010): (1) 80–85 km, (2) 70–75 km, and (3) 60–65 km. Temperature and pressure profiles of the Martian atmosphere that satisfy the median conditions of the detected CO_2 clouds [Ls = 20°; latitude = 0°; longitude = 0°; local time = 16 h] were extracted from the Mars Climate Database 5.2 (Millour et al., 2015). Because the optical properties of the CO_2 ice clouds used in this study are independent of variations in temperature and pressure, we consider only the median atmospheric conditions.

Figure 5 shows typical examples of comparisons between the CO_2 cloud features measured by PFS (the same as in **Fig. 1c**) and the synthetic spectra. In this figure, the synthetic spectra calculated with clouds at altitudes of 80–85 km and effective variance of 0.1 are shown. Our modeling could not reproduce the peak of CO_2 ice with an effective radius of 0.1 μm (**Fig. 5a** and **5e**). The synthetic spectra using Warren RI with an effective radius of 0.5 μm have a peak at 4.27 μm, which is shifted toward longer wavelengths than those measured at 4.25 μm by PFS (**Fig. 5b**). The synthetic spectra using Wood RI with r_{eff} = 0.5 μm and τ = 0.3 - 0.6 are fairly similar to the measured spectra, and these values are close to the previous works by OMEGA (r_{eff} = 1-3 μm, and τ < 0.5 (Määttänen et al. 2010)) and CRISM (r_{eff} = 0.5-2 μm, and τ < 0.3 (Vincendon et al. 2011)). However, the peak positions of the synthetic spectra are slightly shifted toward shorter wavelengths (4.245 μm) than that measured by PFS (4.25 μm), and the secondary peak positions of the synthetic spectra are also slightly shifted toward shorter wavelengths (4.275 μm) than that measured by PFS (4.28 μm) (**Fig. 5f**). With an effective radius larger than 1.0 μm, the synthetic spectra show significantly higher radiance in spectral ranges longer than 4.3 μm, which resulted in failure to reproduce measurements in the corresponding spectral range (**Fig. 5c**, **5d, 5g**, and **5h**). Changing the altitude of the cloud, or the effective variance of the particle size distribution, do not impact the shape of the synthetic spectra (not shown).

5. Discussion of the spectral shapes of the CO_2 ice clouds

We have compared the spectral shapes of mesospheric CO_2 ice clouds measured by PFS and synthetic spectra calculated using a radiative transfer model that assumes a spherical particle shape. As illustrated in **Fig. 5**, although the synthetic spectra with Wood RI, r_{eff} = 0.5 μm, and τ = 0.3-0.6 is fairly similar to the measured spectra, the CO_2 ice cloud features measured by PFS cannot be reproduced by the simulations. This is true for all CO_2 cloud spectra measured by PFS. **Fig. 6** shows the wavelength and intensity of the main peak of the CO_2 ice cloud features measured by PFS, as well as those of the synthetic spectra calculated with the radiative transfer model. In all cases, the main measured peaks occur between 4.24 and 4.265 μm, and none of the synthetic spectra show agreement with those peaks. Montmessin et al. (2007) also pointed out this disagreement. They used a different radiative transfer solver from ours, and calculated single scattering parameters of the CO_2 ice clouds with the Mie theory using the refractive index of Warren (1986). Their modeled peak wavelength was located at 4.28 μm, whereas the peak position observed by OMEGA was shifted by 0.02 μm toward shorter wavelengths (4.26 μm), which is consistent with our results.

In this study, two refractive indices of CO_2 ice measured at temperatures relatively close to those of the Martian mesosphere (Warren, 1986; Wood and Roux, 1982) were used for the Mie scattering calculation. However, none of the calculation results could reproduce the observed peak position, although Wood RI reproduced more similar spectra because of the double peaks (**Fig. 5f**). As shown in **Fig. 4**, the peaks of the real part of the refractive indices are located at 4.277 μm and 4.263 μm for Warren RI and Wood RI, respectively. Because the scattering coefficient at a given wavelength calculated with the Mie theory is a function of the size parameter and complex refractive index, the peak wavelength of the scattering coefficient may differ from that of the real part of index. At the 4.3-μm band, the peaks of the synthetic spectra appear at 4.27 μm with Warren RI and at 4.245 μm and 4.28 μm with Wood RI (double peak) because of a combination of a strong increase in absorption (i.e., the imaginary part of the index) at these spectral ranges and large fluctuation of the real part when the effective radius is smaller than 0.5 μm. The disagreement of the main peak wavelength between measured and synthetic spectra may arise because the available CO_2 ice refractive indices are either inaccurate or inappropriate for the mesospheric temperatures. In fact, the available CO_2 ice refractive indices have large uncertainties in the position and width of the peak at 4.3 μm (Wood and Roux, 1982; Warren, 1986). Moreover, the CO_2 condensation temperature at the altitudes of 60–100 km on Mars ranges from 95 to 120 K (e.g., Listowski et al., 2014), whereas the refractive indices were measured at 65–80 K (Warren, 1986) and 80 K (Wood and Roux, 1982). Warren (1986) pointed out that the positions, strengths, and widths of the lines in the refractive index are generally temperature dependent. Accurate measurements of the refractive index with consideration for temperature dependence are needed to draw a more definitive conclusion. Another possible explanation for the disagreement may be the assumption in our model that the CO_2 ice crystals are spherical and composed by pure CO_2 ice. While there are no observations of the cloud particles shape, the crystal shape is expected to be closer to cubes or octahedrons as suggested by experiments and theoretical works (Foster et al., 1998; Wood, 1999; Mangan et al., 2017), and the nucleation of CO_2 ice crystals is most probably heterogeneous meaning that the crystal properties could be affected by dust grain inclusions (Wood 1999; Colaprete and Toon, 2003; Määttänen et al. 2005; Listowski et al. 2014). Isenor et al. (2013) demonstrated that spectral shape of the 4.3-μm band is variable depending on particle size, shape, and composition (pure and mixed CO_2 aerosol particles) of the CO_2 ice crystal using the discrete dipole approximation (DDA). The PFS spectra cannot be compared with those of their simulation because they showed extinction spectra, which are not comparable to the Nadir PFS spectra but to occultation measurements.

We observed a secondary peak at 4.28 μm eight times out of 111 occurrences. These occurrences have no specific characteristic in observation geometry (such as phase angle, local time, latitude, longitude, and season). Wood RI allows us to reproduce the double peak spectral signature (**Fig. 5f**), however, the modeled peak positions and intensities are not consistent with the observations. **Fig. 7** shows relationships between secondary peak positions and radiances of the measured and synthetic spectra for the eight cases. As shown in this figure, the main peak positions of the synthetic spectra are slightly shifted toward shorter wavelengths (around 4.245 μm) than that measured by PFS (around 4.25 μm), and the secondary peak positions of the synthetic spectra are also slightly shifted toward shorter wavelengths (around 4.275 μm) than that measured by PFS (around 4.28 μm). Although this discrepancy may be related to the characteristics (particle size, shape, and composition) of the mesospheric CO_2 ice clouds, investigating the reason for this secondary peak is beyond the scope of this paper.

The other secondary peak observed by OMEGA (Montmessin et al., 2007) in the spectral range 4.32 μm was not detected from the PFS dataset. This secondary peak is an indication of large particles (effective radius of more than 1 μm (Montmessin et al., 2007), if we assume the shape of the particle is spherical. **Fig. 6** of Määttänen et al. (2010) showed that CO_2 ice clouds with large secondary peaks (the reddish points) are spatially localized: single or a few pixels. The FOV of PFS is about 500 times larger than that of single pixel of OMEGA. Even though we could not give a general statement since **Fig. 6** of Määttänen et al. (2010) is just one example of tens of clouds that have large secondary peaks observed by OMEGA, the horizontal scale of the clouds with secondary peak at 4.32-34 μm may be too small to be detected by PFS.

6. Conclusion

In this study, we have identified 111 occurrences of mesospheric CO_2 ice clouds at the bottom of the 4.3-μm CO_2 band from PFS measurements over the period from MY 27 to MY 32. Detections of CO_2 ice clouds were compared with those observed by OMEGA (Määttänen et al., 2010; Vincendon et al., 2011) and all cases of simultaneous observations (51 cases) were also confirmed by OMEGA data. The spatial distribution of the mesospheric CO_2 ice clouds shows that they occur within the longitudinal range of −100.6°E to +23.2°E (109 cases) and around +161°E (2 cases) over the equatorial latitudes (15.6°S–21.5°N). The seasonal distribution indicates that they occurred within the seasonal range of *Ls* = 8.9° to 134.6°, concentrated between *Ls* = 10° and 30° (87 cases). The season and locations in which mesospheric CO_2 ice clouds were detected are consistent with previous spectroscopic observations (Määttänen et al., 2010; Vincendon et al., 2011). Moreover, mesospheric CO_2 ice clouds were found preferentially in the spectra taken in the late afternoon (15–16 h) in MY 29 even though this cannot be generalized because of the observational biases.

The high spectral resolution of PFS enables us to resolve the spectral shape of CO_2 ice clouds for the first time. In all cases, the CO_2 ice scattering peak is located at 4.25 μm (between 4.240 and 4.265 μm), which is consistent with observation by OMEGA (Monemessin et al., 2007). Moreover, a small secondary peak is found around 4.28 μm (eight occurrences), which was not resolved by OMEGA. The other secondary peak observed by OMEGA (Montmessin et al., 2007) in the spectral range 4.32–4.34 μm was not detected by PFS. We have compared the spectral shapes of mesospheric CO_2 ice clouds measured by PFS and synthetic spectra calculated using a radiative transfer model that assumes a spherical particle shape. Two refractive indices of CO_2 ice measured at temperatures relatively close to those for the Martian mesosphere (Warren, 1986; Wood and Roux, 1982) were used for the Mie scattering calculation. The synthetic spectra with Wood RI, r_{eff} = 0.5 μm and τ = 0.3-0.6 is more similar to the measured spectra and only Wood RI allows to reproduce a double peak structure like the one detected in a few spectra. However, none of the calculated synthetic spectra show agreement with the measured shape of the spectra and positions of the peaks. This disagreement may be because (1) the available CO_2 ice refractive indices are either inaccurate or inappropriate for the mesospheric temperatures, or (2) because of the assumption in our model that the CO_2 ice crystals are spherical and composed by pure CO_2 ice.

The discrete dipole approximation (DDA), which is widely used for non-spherical particles modeling in astronomy and planetary science and was used in the simulation demonstrated by Isenor et al. (2013), would allow us to model IR spectra of non-spherical crystals to be compared with the PFS spectra. Detailed comparison between the measured PFS spectra and those modeled by the DDA can provide new insight on the microphysical characteristics of these mesospheric CO_2 ice clouds.

Acknowledgements

This work has been supported by the European Union Seventh Framework Programme (FP7/2007-2013) under grant agreement n° 607177, FNRS "CRAMIC" project under grant agreement n° T.0171.16, a Grant-in-Aid for Scientific Research (22340142, 24403007, 15H05209, 16K05566) from the Japanese Society for the Promotion of Science (JSPS), and the Tohoku University Global COE program "Global Education and Research Center for Earth and Planetary Dynamics". Mars Express (MEx) has been operated by the ESA, and we are grateful to the MEx-SGS team for their support. The Mars Climate Database 5.2 is provided by F. Forget and E. Millour. The MEx/OMEGA data set was obtained from the Planetary Data System (PDS).

Reference

Bibring, J-P., Soufflot, A., Berthé, M., Langevin, Y., Gondet, B., Drossart, P., Bouyé, M., Combes, M., Puget, P., Semery, A., Bellucci, G., Formisano, V., Moroz, V., Kottsov, V., the OMEGA Co-I team. 2004. OMEGA: Observatoire pour la Mine´ralogie, l'Eau, les Glaces et l'Activite´, in Mars Express: The Scientific Payload, Eur. Space Agency Spec. Publ., ESA-SP 1240, 37–50.

Clancy, R.T., Sandor, B.J., 1998. CO_2 ice clouds in the upper atmosphere of Mars. Geophys. Res.

Lett. 25 (4), 489–492.

Colaprete, A., and Toon O.B., 2003. Carbon dioxide clouds in an early dense Martian atmosphere. Journal of Geophysical Research (Planets), Volume 108, Issue E4, pp. 6-1

Foster, J.L., Chang, A.T.C., Hall, D.K., Wergin, W.P., Erbe, E.F., Barton, J., 1998. Carbon dioxide crystals: An examination of their size, shape, and scattering properties at 37 GHz and comparisons with water ice (snow) measurements. Journal of Geophysical Research, Volume 103, Issue E11, p. 25839-25850

Formisano, V., Angrilli, F., Arnold, G., Atreya, S., Bianchini, G., Biondi, D., Blanco, A., Blecka, M.I., Coradini, A., Colangeli, L., Ekonomov, A., Esposito, F., Fonti, S., Giuranna, M., Grassi, D., Gnedykh, V., Grigoriev, A., Hansen, G., Hirsh, H., Khatuntsev, I., Kiselev, A., Ignatiev, N., Jurewicz, A., Lellouch, E., Lopez Moreno, J., Marten, A., Mattana, A., Maturilli, A., Mencarelli, E., Michalska, M., Moroz, V., Moshkin, B., Nespoli, F., Nikolsky, Y., Orfei, R., Orleanski, P., Orofino, V., Palomba, E., Patsaev, D., Piccioni, G., Rataj, M., Rodrigo, R., Rodriguez, J., Rossi, M., Saggin, B., Titov, D., Zasova, L., 2005. The Planetary Fourier Spectrometer (PFS) onboard the European Mars Express mission. Planet. Space Sci. 53 (10), 963–974.

Formisano, V., Maturilli, A., Giuranna, M., D'Aversa, E., Lopez-Valverde, M.A., 2006. Observations of non-LTE emission at 4-5 microns with the planetary Fourier spectrometer aboard the Mars Express mission, Icarus, 182, 51–67.

Fiorenza, C., Formisano, V., 2005. A solar spectrum for PFS data analysis. Planet. Space Sci. 53, 1009–1016.

Giuranna, M., Formisano, V., Biondi, D., Ekonomov, A., Fonti, S., Grassi, D., Hirsch, H., Khatuntsev, I., Ignatiev, N., Michalska, M., Mattana, A., Maturilli, A., Mencarelli, E., Nespoli, F., Orfei, R., Orleanski, P., Piccioni, G., Rataj, M., Saggin, B., Zasova, L., 2005a. Calibration of the Planetary Fourier Spectrometer long wavelength channel. Planet. Space Sci. 53 (10), 993–1007.

Giuranna, M., Formisano, V., Biondi, D., Ekonomov, A., Fonti, S., Grassi, D., Hirsch, H., Khatuntsev, I., Ignatiev, N., Michalska, M., Mattana, A., Maturilli, A., Moshkin, B.E., Mencarelli, E., Nespoli, F., Orfei, R., Orleanski, P., Piccioni, G., Rataj, M., Saggin, B., Zasova, L., 2005b. Calibration of the Planetary Fourier Spectrometer short wavelength channel. Planet. Space Sci. 53 (10), 975–991.

González-Galindo, F., Määttänen, A., Forget, F., Spiga, A., 2011. The martian mesosphere as revealed by CO_2 cloud observations and general circulation modeling. Icarus 216, 10–22.

Grassi, D., Fiorenza, C., Zasova, L.V., Ignatiev, N.I., Maturilli, A., Formisano, V., Giuranna, M., 2005. The martian atmosphere above great volcanoes: early planetary fourier spectrometer observations, Planet. Space Sci., 53, 1017-1034.

Grassi, D., Ignatiev, N.I., Zasova, L.V., Maturilli, A., Formisano, V., Bianchini, G.A., Giuranna, M., 2005b. Methods for the analysis of data from the Planetary Fourier Spectrometer on the Mars Express mission. Planet. Space Sci., 53, 1053-1064.

Herr, K. C., and Pimentel, G. C., 1970. Evidence for solid carbon dioxide in the upper atmosphere of Mars, Science, 167, 47–49,

Ignatiev, N.I., Grassi, D., Zasova, L.V., 2005. Planetary Fourier spectrometer data analysis: fast radiative transfer models. Planet. Space Sci. 53, 1035–1042.

Isenor, M, Escribano, R., Preston, T.C., Signorell, R., 2013. Predicting the infrared band profiles for CO_2 cloud particles on Mars. Icarus, 223, 591–601.

Kahre M.A., Hollingsworth, J.L., Haberle, R.M., Murphy, J.R., 2008. Investigations of the variability of dust particle sizes in the martian atmosphere using the NASA Ames General

Circulation Model, Icarus, 195, 576-597

Kuntz, M., 1997. A new implementation of the Humlicek algorithmfor the calculation of the Voigt profile function. J. Quant. Spectrosc. Radiat. Transfer 57 (6), 819–824.

Lellouch, E., Encrenaz T., de Graauw T., Erard S., Morris P., Crovisier J., Feuchtgruber H., Girard T., Burgdorf M., 2000. The 2.4– 45 mm spectrum of Mars observed with the infrared space observatory, Planet. Space Sci., 48, 1393–1405.

Lewis S.R. and Steele, L.J., 2014. High-Altitude Dust in the Martian Atmosphere, Mars Modeling and Observations Workshop, London, 2014

Listowski, C., Määttänen, A., Montmessin, F., Spiga, A., Lefevre, F., 2014. Modeling the microphysics of CO_2 ice clouds within wave-induced cold pockets in the Martian mesosphere, Icarus, 237, 239–261.

Määttänen, A., Vehkamäki, H., Lauri, A., Merikallio, S., Kauhanen, J., Savijärvi, H., Kulmala, M., 2005. Nucleation studies in the Martian atmosphere. Journal of Geophysical Research, Volume 110, Issue E2, CiteID E02002.

Määttänen, A., Montmessin, F., Gondet, B., Scholten, F., Hoffmann, H., González- Galindo, F., Spiga, A., Forget, F., Hauber, E., Neukum, G., Bibring, J.-P., Bertaux, J.-L., 2010. Mapping the mesospheric CO_2 clouds on Mars: MEx/OMEGA and MEx/HRSC observations and challenges for atmospheric models. Icarus 209, 452–469.

Mangan, T.P., Salzmann, C.G., Plane, J.M.C., Murray, B.J., 2017. CO2 ice structure and density under Martian atmospheric conditions. Icarus, Volume 294, p. 201-208.

Millour, E. et al., 2015. The Mars Climate Database (MCD version 5.2). European Planetary Science Congress 2015, id.EPSC2015-438.

Montmessin, F., Bertaux, J.-L., Quémerais, E., Korablev, O., Rannou, P., Forget, F., Perrier, S., Fussen, D., Lebonnois, S., Rébérac, A., Dimarellis, E., 2006. Subvisible CO_2 ice clouds detected in the mesosphere of Mars. Icarus 183, 403–410.

Montmessin, F., Gondet, B., Bibring, J.-P., Langevin, Y., Drossart, P., Forget, F., 2007. Hyperspectral imaging of convective CO_2 ice clouds in the equatorial mesosphere of Mars. J. Geophys. Res. 112 (E11S90), 1–14.

Rothman, L.S., Gordon, I.E., Babikov, Y., Barbe, A., Chris Benner, D., Bernath, P.F., Birk, Bizzocchi, L., Boudon, V., Brown, L.R, Campargue, A., Chance, K., Cohen, E.A., Coudert, L.H., Devi, V.M., Drouin, B.J., Fayt, A., Flaud, J.-M., Gamache, R.R., Harrison, J.J., Hartmann, J.-M., Hill, C., Hodges, J.T., Jacquemart, D., Jolly, A., Lamouroux, J., Le Roy, R.J., Li, G., Long, D.A., Lyulin, O.M., Mackie, C.J., Massie, S.T., Mikhailenko, S., 2013. The HITRAN2012 molecular spectroscopic database. J. Quant. Spectrosc. Radiat. Transfer 130, 4-50.

Ruyten, W., 2004. Comment on ‘‘A new implementation of the Humlicek algorithm for the calculation of the Voigt profile function’’ by M. Kuntz [JQSRT 57(6) (1997) 819–824]. J. Quant. Spectrosc. Radiat. Transfer 86, 231–233.

Schofield, J.T. et al., 1997. The Mars pathfinder atmospheric structure investigation/ meteorology (ASI/MET) experiment. Science 278, 1752–1757.

Scholten, F., Hoffmann, H., Määttänen, A., Montmessin, F., Gondet, B., Hauber, E., 2010. Concatenation of HRSC colour and OMEGA data for the determination and 3d-parameterization of high-altitude CO_2 clouds in the martian atmosphere. Planet. Space Sci. 58, 1207–1214.

Spiga, A., González-Galindo, F., López-Valverde, M.-Á., Forget, F., 2012. Gravity waves, cold pockets and CO_2 clouds in the martian mesosphere. Geophys. Res. Lett. 39 (L02201), 1–5.

Smith, M. D., 2009. THEMIS observations of Mars aerosol optical depth from 2002 – 2008, Icarus, 202, 444 – 452.

Vincendon, M., Pilorget, C., Gondet, B., Murchie, S., Bibring, J.-P., 2011. New near-ir observations of mesospheric CO_2 and H_2O clouds on Mars. J. Geophys. Res. 116 (E00J02), 1–30.

Warren, S.G., 1984. Optical constants of ice from the ultraviolet to the microwave. Appl. Opt. 23, 1206–1225.

Wiscombe, W.J., 1980. Improved Mie scattering algorithms. Applied Optics, 19, 9, 1505–1509.

Wolkenberg, P., Giuranna, M., Grassi, D., Aronica, A., Aoki, S., Scaccabarozzi, D., Saggin, B., 2017. Characterization of dust activity on Mars from MY 27 to MY 32 by PFS-MEX observations. Icarus, submitted (under revision).

Wood, B.E., Roux, J.A., 1982. Infrared Optical Properties of Thin H_2O, NH_3, and CO_2 Cryofilms. J. Opt. Soc. Am. 72,720.

Wood, S.E., 1999. Nucleation and growth of carbon dioxide ice crystals in the Martian atmosphere. Thesis (PhD). UNIVERSITY OF CALIFORNIA, LOS ANGELES, Source DAI-B 60/04, p. 1653, Oct 1999, 192 pages.

Figures and Table

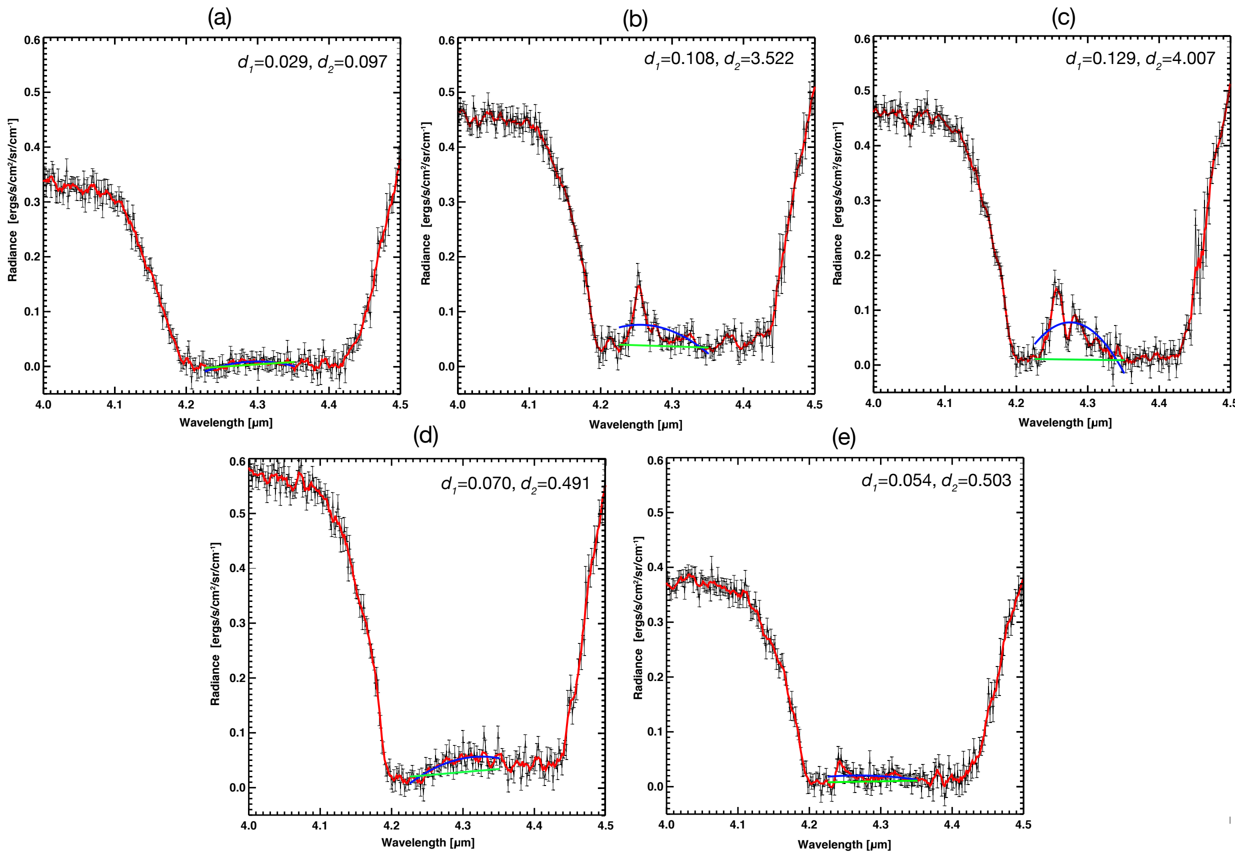

Figure 1: Examples of PFS spectra in the wavelength range between 4.0 μm and 4.5 μm (black curves). The light green and blue curves represent the estimated background radiance and the best-fit quadratic function in the spectral range 4.22–4.35 μm, respectively. The red curves show the smoothed PFS spectra. (a) An example of a PFS spectrum without mesospheric CO_2 ice cloud features (d_1 = 0.029, d_2 = 0.097, orbit #886, latitude = 44.57°N, longitude = 19.44°E, and *Ls* = 93.33°). (b) An example of PFS spectra with mesospheric CO_2 ice cloud features identified by the algorithm (d_1 = 0.108, d_2 = 3.522, orbit # 5267, latitude = 2.88°S, longitude = +17.27°E, and Ls = 28.69°). (c) An example of PFS spectra with mesospheric CO_2 ice cloud features with a secondary peak is found at 4.28 μm (d_1 =0.129, d_2 = 4.007, orbit #5267, latitude = 2.35°S, longitude = +17.27°E, and Ls = 28.69°). (d) An example of a “noisy” PFS spectrum without mesospheric CO_2 ice cloud features (d_1 = 0.070, d_2 = 0.491, orbit #4537, latitude = 8.02°S, longitude = −23.83°E,

and *Ls* = 277.92°). A relatively high noise level provides a large d_1 value, although a distinct scattering peak is not visible. (e) An example of a PFS spectrum with mesospheric CO_2 ice cloud features not detected by algorithm but only by eye (d_1 = 0.054, d_2 = 0.503, orbit #5195, latitude = 7.01°N, longitude = +22.52°E, and Ls = 19.13°). A possible CO_2 ice cloud feature is visible around 4.25 μm.

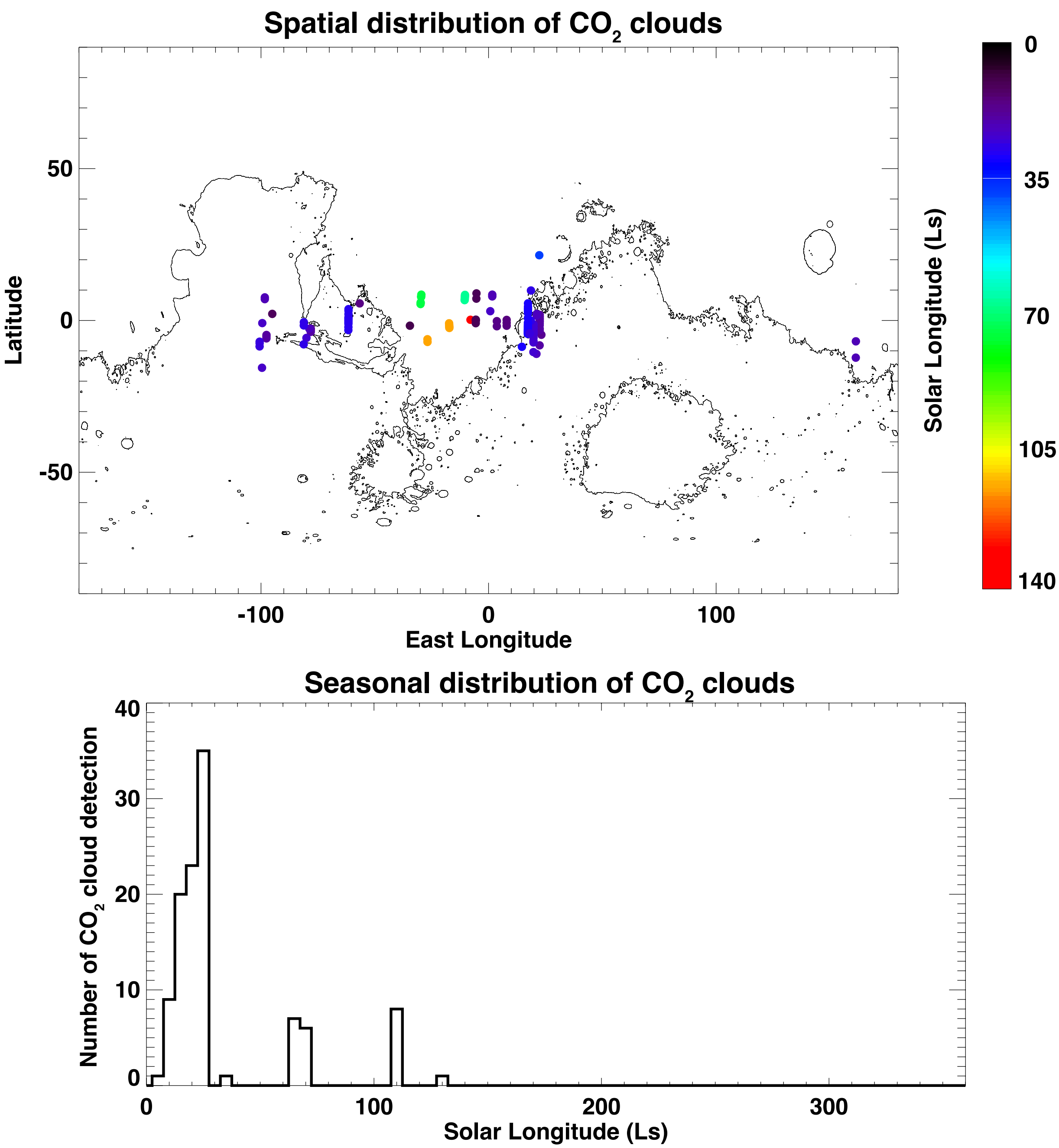

Figure 2: (Top) Spatial distribution of the mesospheric CO_2 ice clouds observed by MEx/PFS. The colors relate to the solar longitude. (Bottom) Seasonal distributions of mesospheric CO_2 ice clouds.

(a)

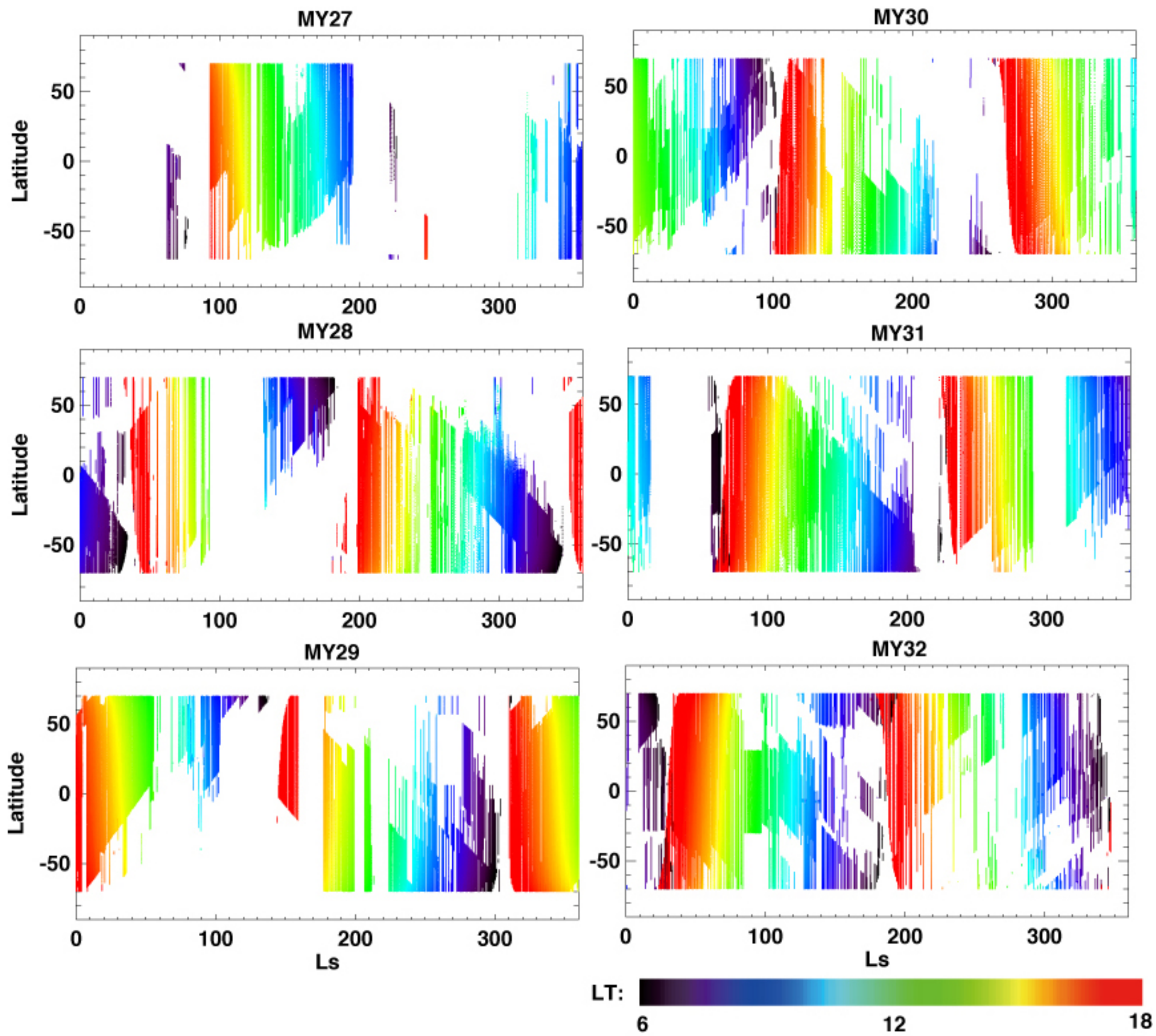

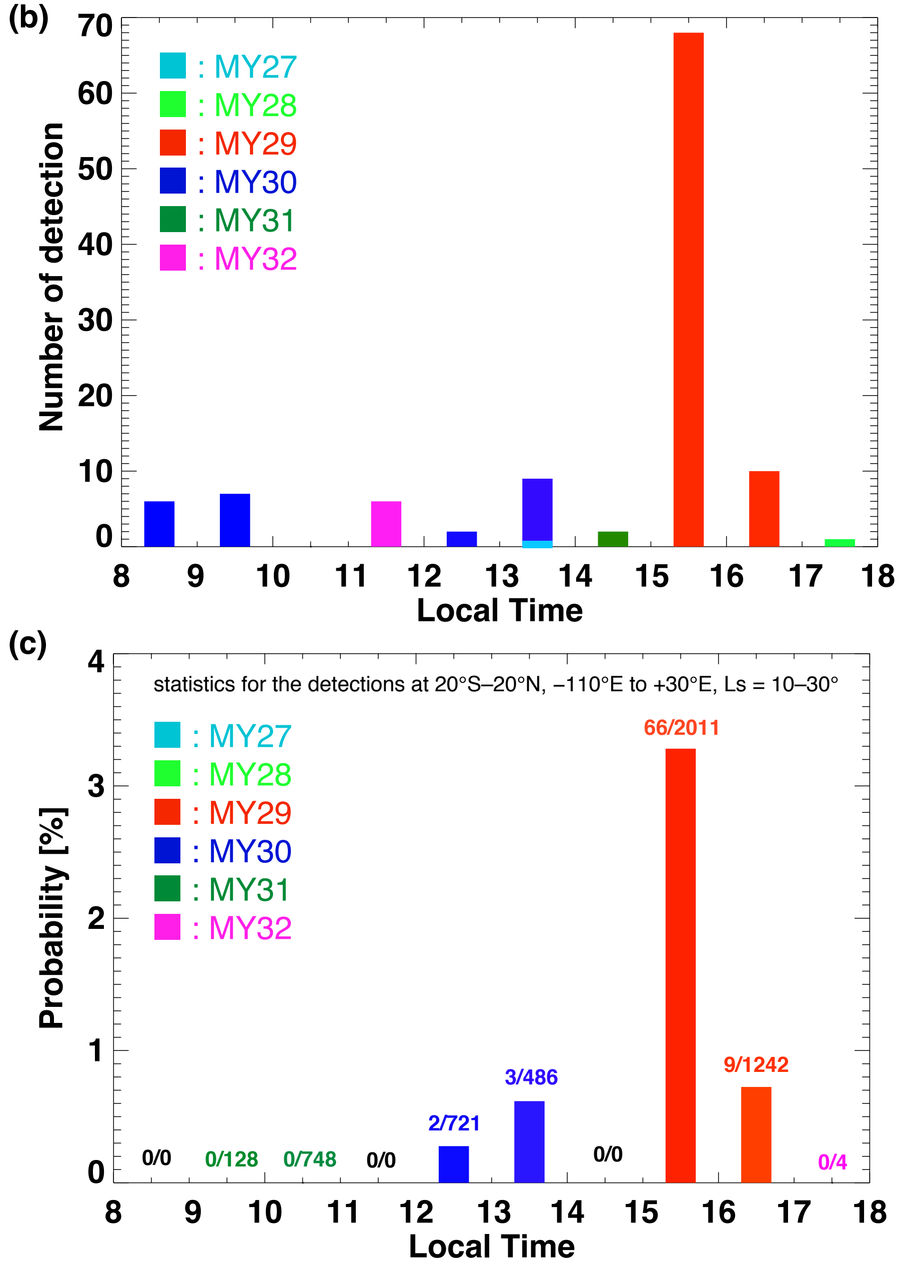

Figure 3: (a) Local time of the PFS spectra used in this study as a function of Ls (x-axis) and latitude (y-axis) in the different MYs (MY27-32). Only daytime observations (between 6 and 18) taken at low-middle latitudes (70°S-70°N) are shown here. (b) Number of mesospheric CO_2 ice clouds detected by PFS at 1-h intervals between 8 and 18 h. (c) Detection probability of mesospheric CO_2 ice clouds at 1-h intervals between 8 and 18 h. In panel c, only detections within the latitudes of 20°S–20°N, longitudes of −110°E to +30°E, and season of *Ls* = 10–30° were used

for these statistics to exclude observational biases. Differences in color represent the observational MY.

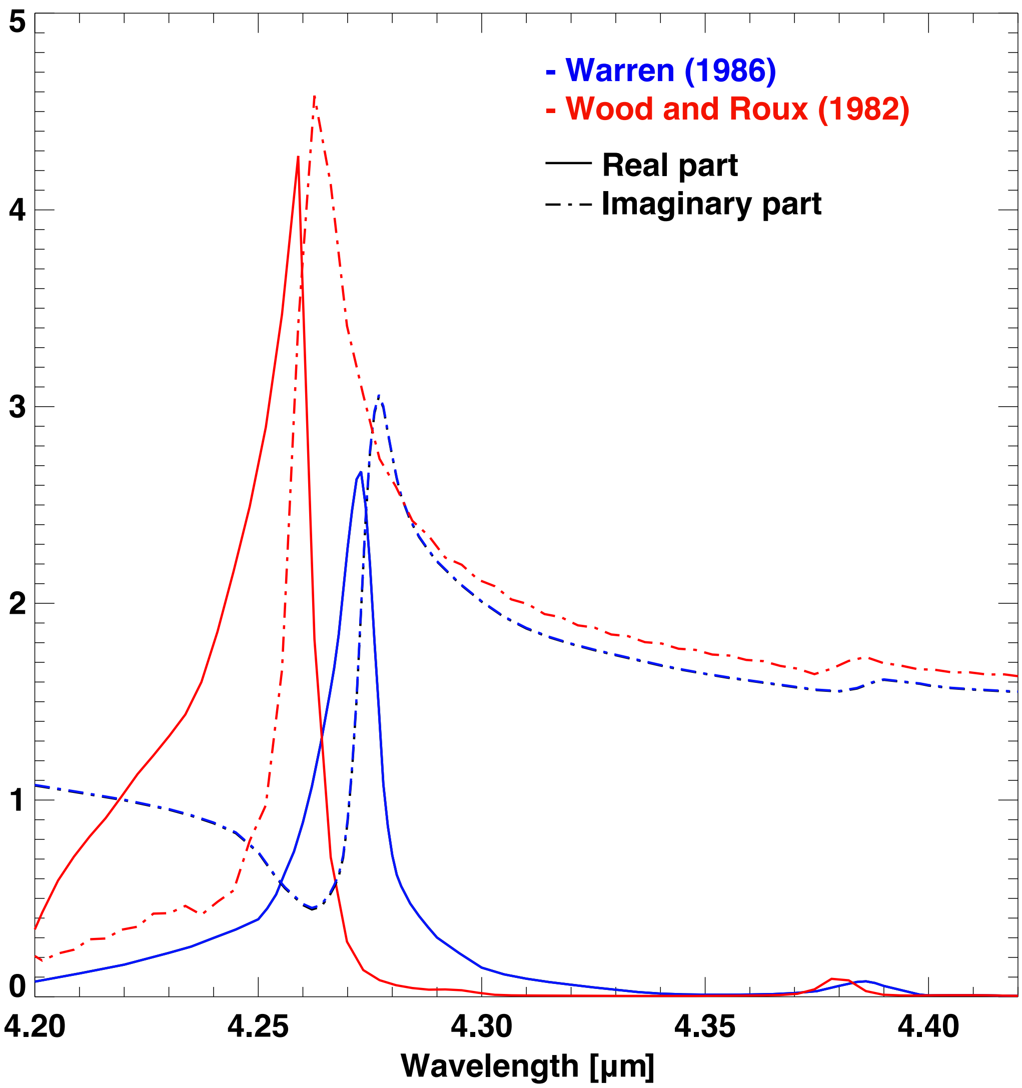

Figure 4: Refractive indices of CO_2 ice used for the Mie scattering calculation performed in this study. The red and blue curves represent the indices by Warren (1986) and by Wood and Roux (1982), respectively. The solid curves indicate the real parts of the indices, and the dashed curves represent the imaginary parts.

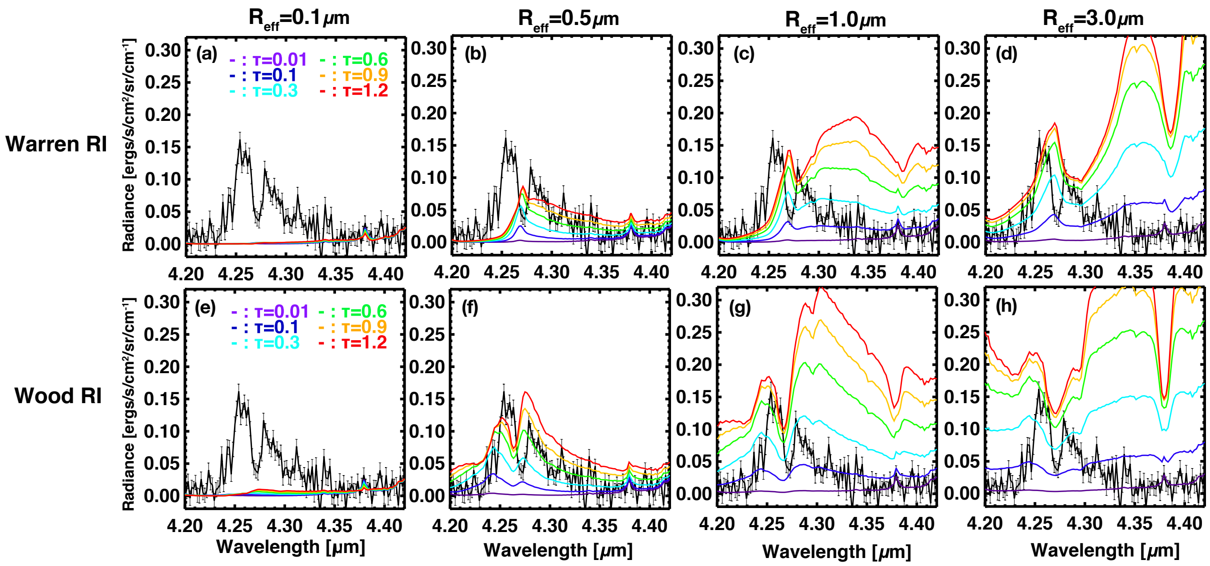

Figure 5: Examples of the comparison between measured mesospheric CO_2 ice cloud spectral features and synthetic spectra calculated using the CO_2 ice refractive indices of Warren (1986) (Figs. a–d) and Wood and Roux (1982) (Figs. e–f). The black curves show a typical example of a CO_2 ice cloud spectrum observed by PFS with a spectrum showing a clear secondary peak at 4.28 μm (same as that shown in Fig. 1c). The synthetic spectra were calculated with various effective radii: r_{eff} = [0.1, 0.5, 1.0, 3.0 μm]. The effective radius v_{eff} of the size distribution is assumed to be 0.1. The purple, blue, light blue, green, orange, and red curves represent the synthetic spectra with optical depths of τ = [0.01, 0.1, 0.3, 0.6, 0.9, 1.2], respectively. Cloud altitudes were assumed to be distributed uniformly within the altitudes of 80–85 km.

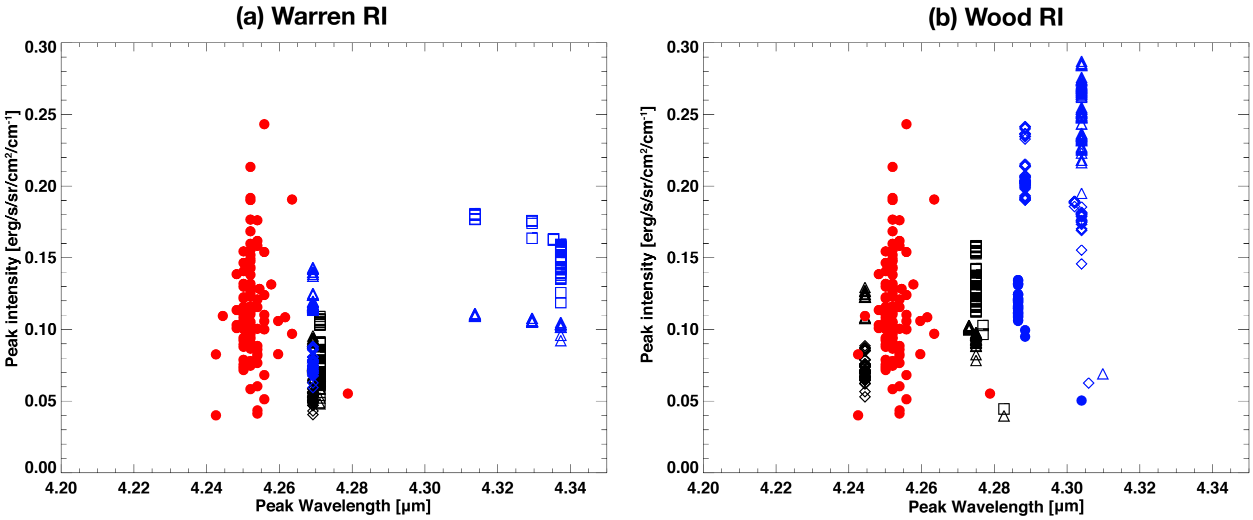

Figure 6: Relationships between main peak positions and radiance of the measured (red) and synthetic spectra (other colors) calculated with (a) the refractive index of Warren (1986), and (b) that of Wood and Roux (1982). The black and blue diamonds, triangles, and squares represent the values of the synthetic spectra with the optical depths of τ = [0.3, 0.6, 0.9] and the effective variance V_{eff} = 0.1 and the effective radius R_{eff} = 0.5 μm (black) and 1.0 μm (blue), respectively.

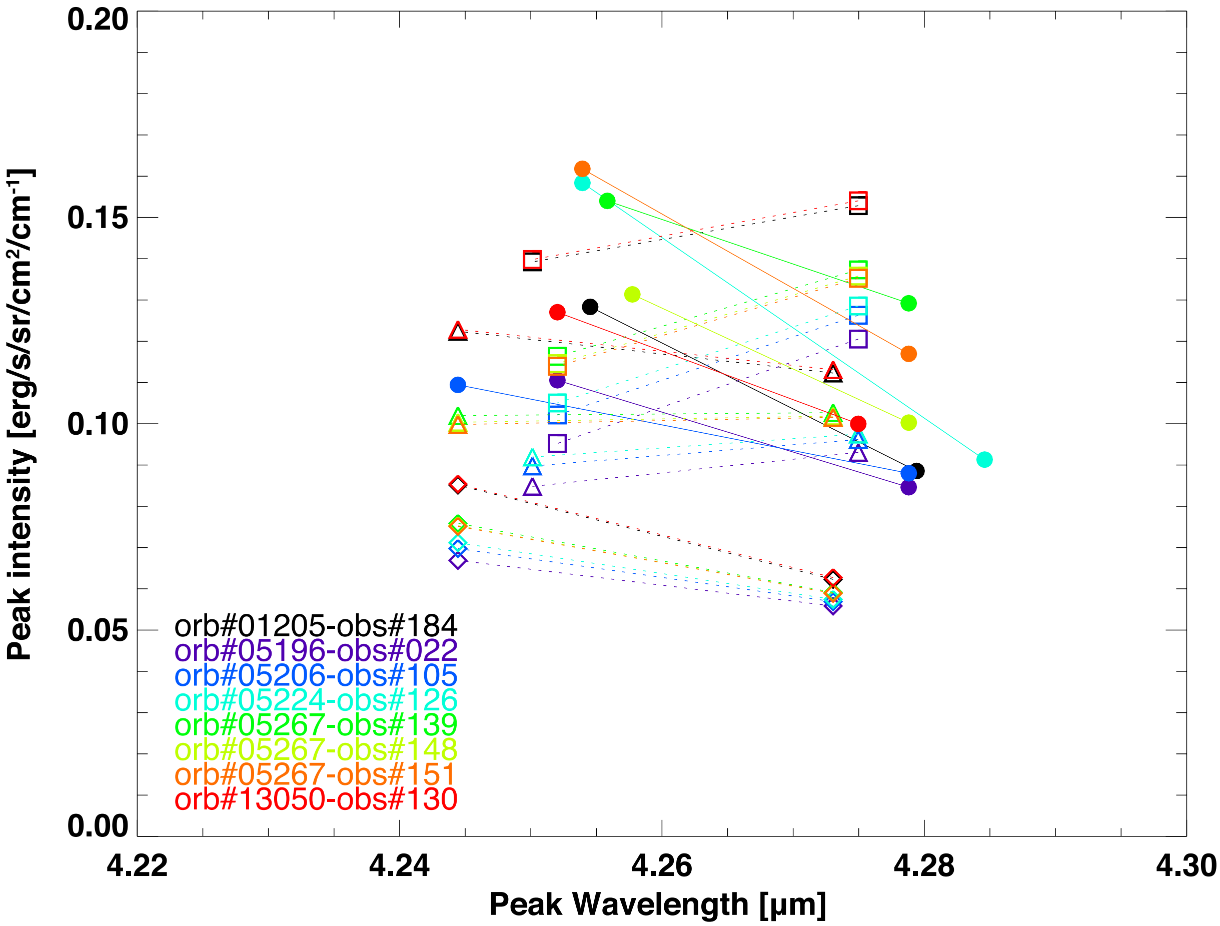

Figure 7: Relationships between secondary peak positions and radiances of the measured (circles) and synthetic (other symbols) spectra for the eight cases (in different colors). The synthetic spectra shown here are those calculated with the refractive index of Wood and Roux (1982), R_{eff} = 0.5 μm and V_{eff} = 0.1. The diamonds, triangles, and squares represent the values of the synthetic spectra with optical depths of τ = [0.3, 0.6, 0.9], respectively. Note that the black and red open symbols (synthetic spectra) sit on the top of each other because solar zenith angles during the observations are similar.

Table 1. List of the mesospheric CO_2 ice clouds detected by PFS during the period from MY 27 to MY 32. The cross symbols in the eighth column indicate that the detections are also confirmed by OMEGA (i.e., reported by Määttänen et al. (2010) and Vincendon et al. (2011)), the minus symbols signify that OMEGA was not operating, and question marks indicate that analysis with the OMEGA data has not yet been reported. The cross symbols in the last column indicate spectra with a secondary peak at 4.28 μm.

MEx Orbit#	**Obs. #**	**Latitude (°N)**	**Longitude (°E)**	**Local Time**	**Martian Year**	**Ls (°)**	**OMEGA Detection**	**4.28 μm Peak**
1205	184	0.22	-7.95	13.5	27	134.59	+	+
2890	312	21.48	22.3	17.87	28	37.91	−	
5120	135	-1.73	-34.56	16.66	29	8.9	+	
5135	134	2.16	-95.06	16.52	29	10.97	−	
5167	139	5.62	-56.64	16.2	29	15.34	−	
5170	150	-0.23	3.65	16.22	29	15.75	+	
5170	153	-1.91	3.64	16.23	29	15.75	+	
5177	160	-4.72	23.22	16.17	29	16.7	+	
5189	128	-4.79	-97.61	16.04	29	18.32	−	
5189	129	-5.35	-97.62	16.04	29	18.32	−	
5189	130	-5.91	-97.62	16.04	29	18.32	−	
5195	115	1.84	22.5	15.97	29	19.13	−	
5195	116	1.26	22.5	15.97	29	19.13	−	

5195	117	0.68	22.49	15.98	29	19.13	−	
5195	118	0.17	22.49	15.98	29	19.13	−	
5195	119	-0.4	22.49	15.98	29	19.13	−	
5195	120	-0.98	22.48	15.98	29	19.13	−	
5195	121	-1.55	22.48	15.99	29	19.13	−	
5195	123	-2.69	22.48	15.99	29	19.13	−	
5195	124	-3.2	22.47	15.99	29	19.13	−	
5195	133	-8.2	22.45	16.01	29	19.13	−	
5196	21	-2.7	-78.14	15.94	29	19.26	−	
5196	22	-3.2	-78.15	15.94	29	19.26	−	+
5196	23	-3.77	-78.15	15.95	29	19.26	−	
5206	105	8.5	1.63	15.82	29	20.6	+	+
5206	106	7.92	1.63	15.82	29	20.6	+	
5207	107	7.6	-98.34	15.82	29	20.74	−	
5207	108	7.02	-98.34	15.82	29	20.74	−	
5208	133	-6.88	161.45	15.86	29	20.87	−	
5208	143	-12.26	161.41	15.89	29	20.87	−	
5213	124	2.17	21.14	15.77	29	21.54	−	
5213	125	1.60	21.14	15.78	29	21.54	−	
5213	148	-11.01	21.05	15.83	29	21.54	−	
5214	134	-2.74	-78.78	15.8	29	21.68	−	
5224	126	3.05	0.76	15.69	29	23.01	+	+

5225	134	-0.87	-99.45	15.68	29	23.14	+	
5225	162	-15.59	-99.57	15.74	29	23.14	+	
5231	2	-1.35	19.79	15.6	29	23.94	+	
5231	4	-2.45	19.78	15.61	29	23.94	+	
5231	6	-3.54	19.77	15.61	29	23.94	+	
5231	7	-4.08	19.77	15.61	29	23.94	+	
5231	8	-4.62	19.76	15.61	29	23.94	+	
5231	10	-5.70	19.75	15.62	29	23.94	+	
5231	12	-6.72	19.74	15.62	29	23.94	+	
5231	13	-7.25	19.74	15.63	29	23.94	+	
5231	19	-10.41	19.71	15.64	29	23.94	+	
5232	145	-5.76	-80.04	15.63	29	24.07	+	
5243	152	-6.99	-100.62	15.54	29	25.53	−	
5243	153	-7.52	-100.62	15.54	29	25.53	−	
5243	155	-8.56	-100.63	15.55	29	25.53	−	
5249	124	9.86	18.63	15.38	29	26.32	−	
5249	142	-0.07	18.58	15.42	29	26.32	−	
5250	143	-0.57	-81.18	15.44	29	26.45	−	
5250	145	-1.65	-81.19	15.44	29	26.45	−	
5250	157	-7.87	-81.25	15.47	29	26.45	−	
5257	137	3.73	-61.56	15.36	29	27.38	+	
5257	138	3.18	-61.56	15.36	29	27.38	+	

5257	140	2.08	-61.57	15.36	29	27.38	+	
5257	142	0.99	-61.58	15.37	29	27.38	+	
5257	143	0.5	-61.58	15.37	29	27.38	+	
5257	144	-0.04	-61.59	15.37	29	27.38	+	
5257	145	-0.58	-61.59	15.37	29	27.38	+	
5257	146	-1.12	-61.6	15.37	29	27.38	+	
5257	148	-2.19	-61.61	15.38	29	27.38	+	
5257	150	-3.19	-61.62	15.38	29	27.38	+	
5267	136	5.63	17.34	15.22	29	28.69	+	
5267	138	4.59	17.34	15.23	29	28.69	+	
5267	139	4.04	17.33	15.23	29	28.69	+	+
5267	140	3.49	17.33	15.23	29	28.69	+	
5267	141	2.95	17.32	15.23	29	28.69	+	
5267	142	2.4	17.32	15.24	29	28.69	+	
5267	145	0.78	17.31	15.24	29	28.69	+	
5267	148	-0.76	17.29	15.25	29	28.69	+	+
5267	149	-1.3	17.29	15.25	29	28.69	+	
5267	150	-1.83	17.28	15.25	29	28.69	+	
5267	151	-2.35	17.27	15.25	29	28.69	+	+
5267	152	-2.88	17.27	15.26	29	28.69	+	
5267	153	-3.4	17.26	15.26	29	28.69	+	
5267	154	-3.92	17.26	15.26	29	28.69	+	

5267	155	-4.44	17.25	15.26	29	28.69	+	
7529	158	8.92	-5.31	13.4	30	10	−	
7529	162	7.18	-5.36	13.41	30	10	−	
7529	179	0.25	-5.59	13.44	30	10	−	
7529	180	-0.12	-5.6	13.44	30	10	−	
7529	182	-0.9	-5.63	13.44	30	10	−	
7561	138	0.18	7.96	13.22	30	14.42	−	
7561	140	-0.79	7.96	13.22	30	14.42	−	
7561	142	-1.75	7.96	13.23	30	14.42	−	
7643	198	-4.27	18.07	12.52	30	25.51	−	
7668	33	-8.68	14.66	12.19	30	28.83	−	
7960	244	8.42	-10.36	9.07	30	66.31	−	
7960	245	8.12	-10.38	9.07	30	66.31	−	
7960	246	7.85	-10.4	9.07	30	66.31	−	
7960	247	7.55	-10.43	9.07	30	66.31	−	
7960	248	7.26	-10.46	9.07	30	66.31	−	
7960	249	6.96	-10.48	9.07	30	66.31	−	
7960	250	6.69	-10.51	9.08	30	66.31	−	
8020	152	8.50	-29.54	8.26	30	73.95	+	
8020	154	7.98	-29.60	8.26	30	73.95	+	
8020	155	7.74	-29.63	8.26	30	73.95	+	
8020	162	5.93	-29.83	8.27	30	73.95	+	

8020	163	5.66	-29.86	8.27	30	73.95	+	
8020	164	5.39	-29.89	8.27	30	73.95	+	
10690	100	-7.08	-26.83	14.2	31	114.51	?	
10690	102	-6.19	-26.86	14.2	31	114.51	?	
13050	127	-2.47	-17.23	11.2	32	114.62	−	
13050	128	-2.14	-17.25	11.2	32	114.62	−	
13050	129	-1.87	-17.27	11.2	32	114.62	−	
13050	130	-1.54	-17.3	11.2	32	114.62	−	+
13050	131	-1.24	-17.32	11.21	32	114.62	−	
13050	132	-0.94	-17.34	11.21	32	114.62	−	

Appendix A. Possible detections of mesospheric CO_2 ice clouds

We have identified 111 occurrences of mesospheric CO_2 ice clouds at the bottom of the 4.3-μm CO_2 band from the PFS dataset using the algorithm described in Section 2.2. However, this algorithm is conservative, and will certainly exclude possible CO_2 cloud detections with weaker signals. Therefore, we have visually inspected the entire PFS dataset to search for other possible CO_2 ice cloud occurrences. As a result, we have identified an additional 175 occurrences that have very similar features to the algorithm detections but were excluded because their signals are weaker and difficult to differentiate from instrumental noise. These visual detections were compared with detections in OMEGA measurements during MY 27–30 (Tables 3 and 4 in Määttänen et al., 2010; Table 3 in Vincendon et al., 2011). There were 167 detections in MY 27–30, and OMEGA performed observations during 73 of these 167 occurrences. We find that OMEGA identified mesospheric CO_2 ice cloud features during all 73 of these occurrences. The list of visual CO_2 ice cloud detections is provided in **Table A1**.

Figure A1 shows the spatial and seasonal distributions of mesospheric CO_2 ice clouds. The visual and algorithm detections are shown together. The distributions are very similar to those of the algorithm detections alone. The spatial distribution shows that the CO_2 ice clouds were detected within the longitudinal range of −100.6°E to +25.2°E (282 cases) and around +161°E (four cases) over the equatorial latitudes ranging from 21.4°S to 21.5°N. The seasonal distribution shows that they occurred in the seasonal range between *Ls* = 3.5° and 134.6°, with most concentrated between *Ls* = 10° and 30° (237 cases). The distribution of these additional detections is in good agreement with that revealed by the previous and current analyses.

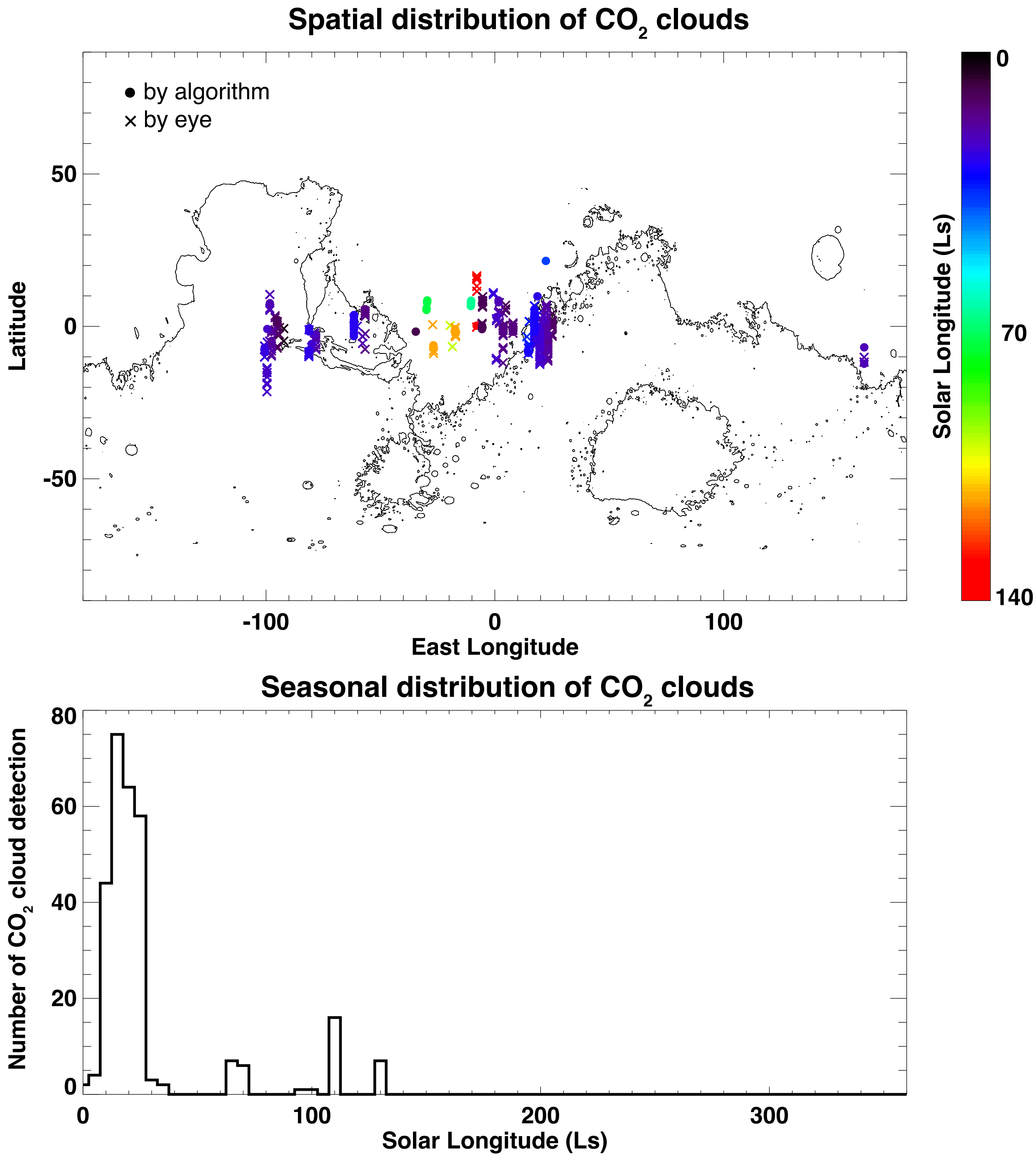

Figure A1: (Top) Spatial and (bottom) seasonal distributions of mesospheric CO_2 ice clouds observed by MExX/PFS. Differences in color in the top map represent the measured solar longitude, and the circle and cross symbols show algorithm and visual detections, respectively.

Table A1: List of mesospheric CO_2 ice clouds detected visually. The cross symbols in the 8th column mean that the detections are also confirmed by OMEGA (i.e., reported in Määttänen et al. (2010) and Vincendon et al. (2011)), the minus symbols represent that OMEGA was not operating, and question marks mean that analysis with the OMEGA data are not yet reported. The cross symbols in the last column indicate spectra with a secondary peak at 4.28 μm.

MEx Orbit#	**Obs. #**	**Latitude (°N)**	**Longitude (°E)**	**Local Time**	**Martian Year**	**Ls (°)**	**OMEGA Detection**	**4.28 μm Peak**
934	292	-6.68	-18.53	16.37	27	99.32	+	
945	284	0.26	-19.5	16.21	27	100.69	+	
1205	154	16.56	-7.9	13.43	27	134.59	+	+
1205	155	15.98	-7.9	13.44	27	134.59	+	
1205	156	15.4	-7.89	13.44	27	134.59	+	
1205	160	13.16	-7.89	13.45	27	134.59	+	
1205	163	11.51	-7.89	13.45	27	134.59	+	
1205	185	-0.25	-7.95	13.5	27	134.59	+	
5081	123	-0.73	-92.24	17.07	29	3.45	−	
5081	130	-4.81	-92.26	17.09	29	3.45	−	
5117	132	-0.35	-94.1	16.71	29	8.48	−	
5117	136	-2.71	-94.11	16.71	29	8.48	−	
5123	124	4.15	25.21	16.6	29	9.31	+	

5134	125	6.94	4.71	16.49	29	10.83	−	
5134	127	5.76	4.71	16.49	29	10.83	−	+
5134	128	5.24	4.71	16.5	29	10.83	−	+
5134	136	0.52	4.69	16.51	29	10.83	−	
5135	135	1.57	-95.06	16.52	29	10.97	−	
5135	137	0.39	-95.07	16.53	29	10.97	−	
5135	138	-0.2	-95.07	16.53	29	10.97	−	
5135	139	-0.78	-95.07	16.53	29	10.97	−	
5135	142	-2.55	-95.08	16.54	29	10.97	−	
5135	149	-6.57	-95.1	16.55	29	10.97	−	
5135	150	-7.15	-95.1	16.56	29	10.97	−	
5141	136	1.98	25.11	16.49	29	11.79	+	
5141	137	1.39	25.11	16.49	29	11.79	+	
5141	138	0.8	25.11	16.5	29	11.79	+	
5141	139	0.21	25.1	16.5	29	11.79	+	
5141	140	-0.38	25.1	16.5	29	11.79	+	
5141	144	-2.65	25.09	16.51	29	11.79	+	
5141	145	-3.24	25.09	16.51	29	11.79	+	
5153	138	3.48	-96.01	16.34	29	13.44	−	
5153	139	2.89	-96.01	16.34	29	13.44	−	
5153	146	-1.15	-96.03	16.36	29	13.44	−	+
5153	147	-1.73	-96.04	16.36	29	13.44	−	

5159	151	-2.56	24.16	16.34	29	14.26	−	
5167	140	5.04	-56.65	16.2	29	15.34	−	
5167	141	4.45	-56.65	16.2	29	15.34	−	
5167	142	3.93	-56.65	16.21	29	15.34	−	
5167	143	3.34	-56.65	16.21	29	15.34	−	
5167	153	-2.41	-56.68	16.23	29	15.34	−	+
5167	162	-7.5	-56.71	16.25	29	15.35	−	
5170	142	4.37	3.67	16.21	29	15.75	+	
5170	149	0.35	3.65	16.22	29	15.75	+	
5170	151	-0.75	3.65	16.23	29	15.75	+	
5170	152	-1.33	3.64	16.23	29	15.75	+	
5170	154	-2.48	3.64	16.23	29	15.75	+	
5170	155	-3.06	3.64	16.24	29	15.75	+	
5170	162	-6.99	3.62	16.25	29	15.75	+	
5170	163	-7.56	3.61	16.25	29	15.75	+	
5170	171	-11.97	3.6	16.27	29	15.75	+	
5177	158	-3.64	23.22	16.17	29	16.7	+	
5177	161	-5.29	23.21	16.17	29	16.7	+	
5177	162	-5.85	23.21	16.17	29	16.7	+	
5177	163	-6.42	23.21	16.18	29	16.7	+	
5177	164	-6.98	23.21	16.18	29	16.7	+	
5177	165	-7.55	23.2	16.18	29	16.7	+	

5177	170	-10.27	23.19	16.19	29	16.7	+	
5177	171	-10.83	23.19	16.19	29	16.7	+	
5177	172	-11.38	23.19	16.2	29	16.7	+	
5188	106	7.83	2.00	15.97	29	18.19	−	
5188	111	4.97	1.99	15.98	29	18.19	−	
5188	117	1.55	1.97	15.99	29	18.19	−	
5188	118	0.97	1.97	15.99	29	18.19	−	
5189	122	-1.43	-97.59	16.03	29	18.32	−	+
5189	123	-2.01	-97.6	16.03	29	18.32	−	
5189	131	-6.48	-97.62	16.04	29	18.32	−	
5189	134	-8.09	-97.63	16.05	29	18.32	−	
5189	136	-9.2	-97.64	16.06	29	18.32	−	
5189	137	-9.75	-97.64	16.06	29	18.32	−	
5195	106	7.01	22.52	15.95	29	19.13	−	
5195	107	6.43	22.52	15.95	29	19.13	−	
5195	108	5.84	22.52	15.96	29	19.13	−	
5195	110	4.68	22.51	15.96	29	19.13	−	
5195	111	4.16	22.51	15.96	29	19.13	−	
5195	113	3.00	22.5	15.97	29	19.13	−	
5195	114	2.42	22.5	15.97	29	19.13	−	
5195	122	-2.12	22.48	15.99	29	19.13	−	
5195	125	-3.77	22.47	15.99	29	19.13	−	

5195	126	-4.33	22.47	16	29	19.13	−	
5195	127	-4.9	22.47	16	29	19.13	−	
5195	128	-5.46	22.46	16	29	19.13	−	
5195	129	-6.02	22.46	16	29	19.13	−−	
5195	130	-6.52	22.46	16	29	19.13	−	
5195	132	-7.64	22.45	16.01	29	19.13	−	
5195	135	-9.31	22.44	16.02	29	19.13	−	
5196	27	-6.03	-78.17	15.96	29	19.26	−	
5196	29	-7.15	-78.17	15.96	29	19.26	−	
5196	30	-7.65	-78.18	15.96	29	19.26	−	
5203	122	-3.31	-57.79	15.92	29	20.2	+	
5203	126	-5.57	-57.8	15.93	29	20.2	+	
5206	112	4.5	1.61	15.83	29	20.6	+	
5207	102	10.45	-98.33	15.81	29	20.74	−	
5207	110	5.86	-98.35	15.83	29	20.74	−	
5207	111	5.28	-98.35	15.83	29	20.74	−	
5207	129	-4.81	-98.41	15.87	29	20.74	−	
5207	133	-7.01	-98.43	15.88	29	20.74	−	+
5208	139	-10.13	161.43	15.88	29	20.87	−	
5208	142	-11.73	161.42	15.88	29	20.87	−	
5213	122	3.25	21.15	15.77	29	21.54	−	
5213	126	1.03	21.13	15.78	29	21.54	−	

5214	133	-2.18	-78.78	15.79	29	21.68	−	
5214	137	-4.4	-78.79	15.8	29	21.68	−	
5224	127	2.49	0.75	15.69	29	23.01	+	
5224	128	1.92	0.75	15.69	29	23.01	+	
5224	151	-10.51	0.66	15.74	29	23.01	+	
5224	152	-11.04	0.65	15.74	29	23.01	+	
5225	142	-5.22	-99.49	15.7	29	23.14	+	
5225	158	-13.61	-99.56	15.74	29	23.14	+	
5225	159	-14.13	-99.56	15.74	29	23.14	+	
5225	161	-15.14	-99.57	15.74	29	23.14	+	
5225	164	-16.6	-99.58	15.75	29	23.14	+	
5225	168	-18.58	-99.59	15.76	29	23.14	+	
5225	169	-19.07	-99.6	15.76	29	23.14	+	
5225	174	-21.43	-99.61	15.77	29	23.14	+	
5231	1	-0.79	19.79	15.6	29	23.94	+	
5231	3	-1.9	19.78	15.6	29	23.94	+	
5231	5	-2.99	19.78	15.61	29	23.94	+	
5231	9	-5.17	19.76	15.62	29	23.94	+	
5231	11	-6.24	19.75	15.62	29	23.94	+	
5231	14	-7.78	19.73	15.63	29	23.94	+	
5231	15	-8.31	19.73	15.63	29	23.94	+	
5231	17	-9.36	19.72	15.63	29	23.94	+	

5231	18	-9.88	19.71	15.64	29	23.94	+	
5231	20	-10.92	19.7	15.64	29	23.94	+	
5231	21	-11.44	19.7	15.64	29	23.94	+	
5231	22	-11.96	19.69	15.64	29	23.94	+	
5231	23	-12.47	19.69	15.65	29	23.94	+	
5232	147	-6.83	-80.05	15.63	29	24.07	+	
5239	137	0.06	-60.14	15.56	29	25	+	
5242	119	11.04	-0.65	15.46	29	25.4	+	
5242	120	10.47	-0.66	15.46	29	25.4	+	
5243	151	-6.47	-100.61	15.54	29	25.53	−	
5243	158	-10.05	-100.65	15.55	29	25.53	−	
5249	135	3.72	18.6	15.41	29	26.32	−	
5249	144	-1.16	18.57	15.43	29	26.32	−	
5250	144	-1.11	-81.18	15.44	29	26.45	−	
5250	158	-8.39	-81.25	15.47	29	26.45	−	
5250	159	-8.9	-81.26	15.47	29	26.45	−	
5250	160	-9.41	-81.26	15.47	29	26.45	−	
5250	161	-9.92	-81.27	15.47	29	26.45	−	
5257	139	2.63	-61.56	15.36	29	27.38	+	
5267	134	6.74	17.35	15.22	29	28.69	+	
5267	143	1.86	17.31	15.24	29	28.69	+	
5267	145	1.32	17.31	15.24	29	28.69	+	

5303	156	1.6	15.05	14.91	29	33.39	−	
5303	171	-5.81	14.95	14.94	29	33.39	−	
5303	172	-6.29	14.94	14.94	29	33.39	−	
5321	138	-3.37	14.01	14.78	29	35.72	+	
7529	156	9.76	-5.28	13.4	30	10	−	
7529	159	8.46	-5.32	13.4	30	10	−	
7529	160	8.04	-5.33	13.41	30	10	−	
7529	163	6.72	-5.37	13.41	30	10	−	
7529	164	6.32	-5.38	13.41	30	10	−	
7529	177	0.99	-5.56	13.44	30	10	−	
7529	178	0.62	-5.58	13.44	30	10	−	
7561	136	1.14	7.96	13.21	30	14.42	−	
7561	137	0.63	7.96	13.22	30	14.42	−	
7561	139	-0.33	7.96	13.22	30	14.42	−	
7561	141	-1.3	7.96	13.23	30	14.42	−	
7561	143	-2.26	7.96	13.23	30	14.42	−	
7643	199	-4.71	18.07	12.52	30	25.51	−	
7643	200	-5.11	18.07	12.53	30	25.51	−	
7643	201	-5.56	18.08	12.53	30	25.51	−	
7643	202	-5.96	18.08	12.53	30	25.51	−	
7668	26	-7.07	14.8	12.18	30	28.83	+	
7668	27	-7.31	14.78	12.18	30	28.83	+	

7668	34	-8.89	14.65	12.19	30	28.83	+	
10690	96	-8.89	-26.77	14.19	31	114.51	?	
10690	98	-7.98	-26.8	14.2	31	114.51	?	
10690	118	0.54	-27.13	14.23	31	114.51	?	
13050	124	-3.38	-17.16	11.2	32	114.62	?	
13050	125	-3.08	-17.19	11.2	32	114.62	?	
13050	126	-2.78	-17.21	11.2	32	114.62	?	
13050	133	-0.64	-17.36	11.21	32	114.62	?	
13050	134	-0.34	-17.38	11.21	32	114.62	?	